

pubs.acs.org/cm Article

Impact of Ni-Mn-Co-Al-Based Cathode Material Composition on the Sintering with Garnet Solid Electrolytes for All-Solid-State **Batteries**

Alexander Bauer, Christoph Roitzheim, Sandra Lobe, Yoo Jung Sohn, Doris Sebold, Walter Sebastian Scheld, Martin Finsterbusch, Olivier Guillon, Dina Fattakhova-Rohlfing, and Sven Uhlenbruck*



Cite This: Chem. Mater. 2023, 35, 8958-8968



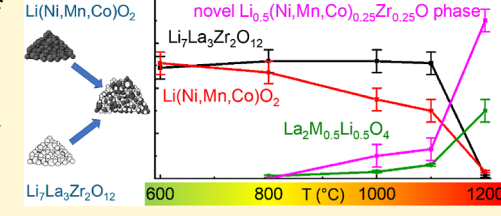
ACCESS I

Metrics & More

Article Recommendations

Supporting Information

ABSTRACT: A systematic and comprehensive study of the thermal stability of Li(Ni,Mn,Co)O₂ the cathode active materials LiNi_{1/3}Mn_{1/3}Co_{1/3}O₂ (NMC111), Li-Ni_{0.6}Mn_{0.2}Co_{0.2}O₂ (NMC622), LiNi_{0.8}Mn_{0.1}Co_{0.1}O₂ (NMC811), and Li-Ni_{0.8}Co_{0.15}Al_{0.05}O₂ (NCA) in combination with the garnet solid electrolyte Li_{6.45}La₃Zr_{1.6}Ta_{0.4}Al_{0.05}O₁₂ was performed, and the respective thermal stability limits in air were assessed. Compared to prior studies on such material mixtures, additional Zr-containing secondary phases were detected, which had not been taken into consideration in a previously published work. Here, these phases were



successfully identified for the first time by a combination of X-ray diffraction, Raman spectroscopy, and microstructural analysis.

■ INTRODUCTION

The garnet family Li-ion conductors related to Li₇La₃Zr₂O₁₂ are attracting considerable attention as a solid electrolyte for inorganic solid-state batteries due to their relatively high ionic conductivity of up to 2 mS/cm at 25 °C, processability in air, nonflammability, broad electrochemical stability window, and especially their high reduction stability in combination with lithium metal.¹⁻⁵ Therefore, Li₇La₃Zr₂O₁₂-based garnets have the capability to completely replace the flammable liquid electrolyte in lithium-ion batteries and thus enable all-solidstate batteries (ASBs) with unprecedented cell-level safety and potentially high energy density. The technical challenge in manufacturing garnet-based batteries is the need for heat treatment (sintering) for proper bonding of powder particles and densification, which can exceed temperatures of 1000 °C.6° The high sintering temperatures often lead to material compatibility problems due to the interdiffusion of the elements at the interfaces and the formation of undesirable secondary phases. The problem of material compatibility become particularly important when sintering such oxide solid electrolytes and cathode active materials (CAM) powders, where the formation of secondary phases has been observed at temperatures as low as 400-600 °C.^{7,8}

Among the various CAM compositions, LiCoO₂ (LCO) has been found to be the only one that is thermodynamically stable in combination with Li₇La₃Zr₂O₁₂-based garnets at temperatures up to 1085 °C, although small amounts of secondary phases such as La₂CoO₄, LaCoO₃, La₂Zr₂O₇, Li₂CO₃, and tetragonal or Co-doped garnet were detected already at lower temperatures when different garnet compositions, processing,

and detection methods were used. 7,9-12 Due to this high thermodynamic stability, LCO has been the CAM of choice in the majority of all reported garnet ASBs (ref 7 and reference therein). However, LCO has a relatively low specific capacity of 140 mA h/g, which limits the energy density of a resulting LCO-based ASB. The requirement for high battery performance necessitates the use of high capacity/high voltage CAMs. However, previous work on high voltage (i.e., higher than 5 V) spinel CAMs showed strong decomposition effects during heat treatment at temperatures lower than 800 °C. 13,14 CAMs with the high manganese content have been shown to be particularly susceptible to the disproportionation reaction, i.e., $\text{LiCoMnO}_4 \rightarrow x \text{Li}_2 \text{MnO}_3 + \text{Li}_{1-2x} \text{CoMn}_{1-x} \text{O}_{4-3x-d}^{15,16}$

especially with a surplus of lithium, which leads to the formation of lithium-rich Li₂MnO₃. Li₇La₃Zr₂O₁₂ is often intentionally prepared with an excess of the lithium precursor to reduce lithium loss during heat treatment and mitigate the formation of resistive La₂Zr₂O₇ as a secondary phase. The combination of such spinels and lithium-(over)saturated Li₇La₃Zr₂O₁₂ therefore inherently poses a particularly high risk of decomposition.

 $+\frac{1}{2}dO_{2}$

Received: June 22, 2023 October 11, 2023 Revised: Accepted: October 12, 2023 Published: October 25, 2023





The use of high-voltage CAMs is essential to increasing the energy density of garnet ASBs. In particular, layered CAMs with molecular formula LiNixMnvCozO2 (NMC) and LiNi_xCo_yAl_zO₂ (NCA) are attractive CAMs due to their excellent electrochemical properties, i.e., high voltage and high capacity (>150 mA h/g), lower cobalt content, and lower price. Various compositions of NMC are being investigated as CAMs for garnet-type ASBs, but to the best of our knowledge, there is no previously published work that provides a systematic experimental analysis of the thermal compatibility between Li₇La₃Zr₂O₁₂ and NMC materials of different compositions. The experimental and theoretical studies that were found mostly dealt with single NMC compositions. Moreover, different chemical compositions of the garnet phase were used for different studies, which makes it difficult to systematically compare the reactivity of the materials. ^{6,7,20-24} In addition, a general problem in comparing data from different sources is that certain variations in preparation, such as NMC/garnet ratios, pressure, thermal treatment (heating rates and dwell times), and the choice of a powder bed composition for sintering, can have a significant impact on the results.²⁵ Furthermore, the analytical techniques chosen generally determine the sensitivity and detection limits for identifying the secondary phases formed. This fact and variations in data analysis, such as Rietveld refinement, can lead to significantly different conclusions about the thermodynamic stability of NMC/garnet mixtures in different studies. As a result, there is a large disagreement on the reaction onset temperature (400-750 °C) and the nature of the secondary phases [La(Co, Mn)O₃, La(Co, Ni)O₃, LaNiO₃, La- $Ni_{0.5}Mn_{0.5}O_3$, $LaCo_{1-x}Mn_xO_3$ (x < 0.4), $La_2Zr_2O_7$ and, Li₂CO₃] between different studies, indicating that the stability between CAM and Li₇La₃Zr₂O₁₂ garnet strongly depends on the experimental conditions and thus cannot be unambiguously described by thermodynamic calculations alone. Therefore, the main purpose of this work is to avoid the misleading interpretations mentioned above and to provide points of reference for future experimental and theoretical work on the development of oxide-based ASBs.

The current work continues our earlier study on the thermal compatibility of garnet materials and NMC²⁶ using a similar experimental approach but significantly expanding the number of NMC compositions and the temperature range for cosintering. The previous work investigated the compatibility of garnets with NMC111 and NMC811 during cosintering in a temperature range of 25–1200 $^{\circ}\text{C}$ but only provides a detailed phase analysis after cosintering at 800 °C. By using Ta, Alsubstituted LLZO ("LLZO" in the following) from the same batch and applying identical processing steps, reliable data were obtained on the effects of different NMC compositions on thermal compatibility with LLZO. Based on in situ hightemperature X-ray diffraction (XRD) analysis, scanning electron microscopy (SEM), and energy-dispersive X-ray spectroscopy (EDS), it was possible to identify the onset temperature, type, and amount of secondary phases formed at a moderate temperature of 800 °C. In the case of NMC111 + LLZO, the first secondary phases form at 800 °C were At 800 °C, they form in amounts of 4 and 1 wt %, respectively. In the case of NMC811 + LLZO, the formation of the secondary phases starts at 650 °C, but only La₂(Ni_{0.5}Li_{0.5})O₄ was observed in an amount of 2 wt % at 800 °C. Therefore, in the previous study, Ni-rich NMC811 was considered as the most promising CAM for garnet-type ASBs.²⁶ In this follow-up work, the study was extended to cathode materials NMC622 and NCA, which allowed a detailed investigation of four commercially available NMC compositions in contact with LLZO under exactly the same conditions. The identification and analysis of secondary phase formation, especially with respect to Zr-containing phases, were extended to temperatures up to 1200 °C, and Raman spectroscopy was additionally used to study the phase composition of garnet-based composite cathodes in more detail.

■ EXPERIMENTAL PART

The solid-state electrolyte material with the nominal composition $Li_{6.45}La_3Zr_{1.6}Ta_{0.4}Al_{0.05}O_{12}$ was synthesized via a solid-state reaction process, as described elsewhere. 27 A moderate excess of the lithium precursor (equivalent to a surplus of 10 mol % Li) was added to balance a potential Li loss during preparation/heat treatment. The addition of α -Al₂O₃ was due to providing a sintering additive. The authors assume that part of the Al2O3 may react with a fraction of the lithium precursor, forming a glass-like lithium aluminum oxide phase, which melts at about 1150 °C and can act as a sintering agent. 4,27,28 An increased aluminum content compared to the stoichiometric amount is expected since the powder was synthesized in an alumina crucible.²⁹ LLZ powder of this quality was analyzed in regarding to crystal phase purity, composition, morphology, particle size distribution (typical values: $d_{10} = 0.08 \ \mu\text{m}$, $d_{50} = 2.55 \ \mu\text{m}$, $d_{90} = 5.19 \ \mu\text{m}$) and surface properties in a previous work,^{26,27} and small amounts of a secondary phase La₂Li_{0.5}Al_{0.5}O₄ [Inorganic Crystal Structure Database (ICSD) no. 202439] could be obtained. Other phases like tetragonal LLZO (ICSD 246816) or Li₂CO₃ (ICSD 66941) appeared to be negligible. The CAMs were obtained from commercial suppliers and processed without any further modification together with the LLZO particles. NMC 111 had a particle size distribution characterized by d_{10} = 4.1 μ m, d_{50} = 7.0 μ m, and d_{90} = 11.2 μ m. NMC 622 had a particle size distribution characterized by $d_{10} = 7.2 \ \mu\text{m}$, $d_{50} = 13.1 \ \mu\text{m}$, and $d_{90} = 23.2 \ \mu\text{m}$. NMC811 exhibited values of $d_{10} = 6.2 \ \mu\text{m}$, $d_{50} = 10.1 \ \mu\text{m}$, and $d_{90} = 15.0 \ \mu\text{m}$, while the particle size distribution of NCA had the parameters $d_{10} = 3.9 \mu \text{m}$, d_{50} = 6.1 μ m, and d_{90} = 9.4 μ m (measured by a Retsch/HORIBA LA 950 particle size analyzer). It was found in the literature that the actual composition compared to the nominal composition and phase purity of battery grade CAMs of different manufacturers are in narrow confines; moreover, also the particle size distributions do not vary largely. 26,30-32 It is therefore concluded that the choice of manufacturer for CAM likely does not play a major role but that the handling and processing of/with LLZ does.

The respective active material powders and LLZO were ground with a mortar and pestle for 5 min to deagglomerate electrolyte particles and homogenize the mixture. The chosen mass ratio for the electrolyte and CAM powders, respectively, was 1:1 in each case. Generally, a high contact surface area of the two mixed components is important to study interdiffusion phenomena. On the one hand, taking into consideration the theoretical density of the active materials (4.7 g/cm³)³³ and LLZO (5.3 g/cm³, authors' estimation based on a lattice parameter), the volume of active material is roughly 10% larger than the volume of the electrolyte. On the other hand, the particle size distributions of the materials differ significantly, thus convoluting the effect of the 10% difference in density.

Pellets with a mass of 1 g were pressed with a hydraulic uniaxial press with a die 13 mm in diameter to ensure close contact between the powder particles. The applied pressure of 110 MPa was kept constant for 1 min for each sample. The pellets were placed on a compacted LLZO powder bed on top of a magnesium oxide plate. The samples were then heat treated in an air atmosphere using an alumina crucible and lid. The thermal treatment was carried out with a heating rate of 5 K/min and a holding time of 1 h, followed by free cooling. A holding time of 1 h was selected (i) to allow a comparison with previous work 13 and (ii) because holding times in the range from

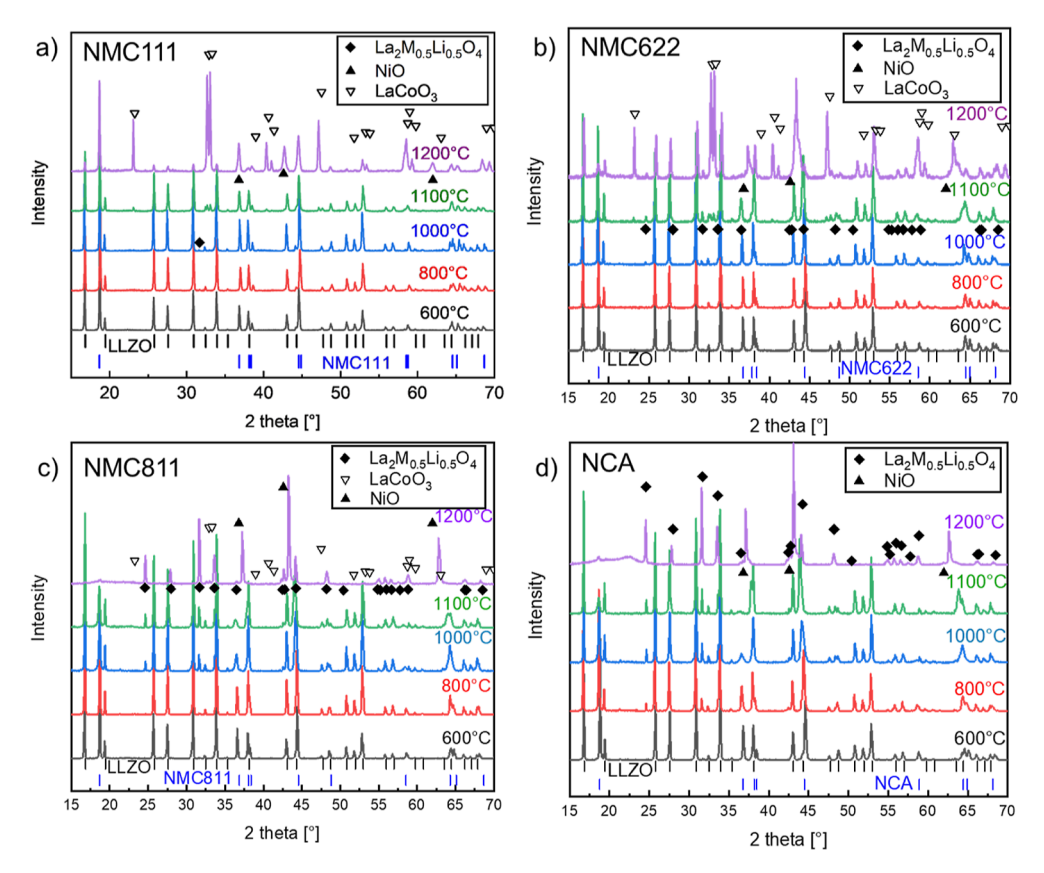


Figure 1. XRD patterns of mixtures of: (a) NMC111 and LLZO; (b) NMC622 and LLZO; (c) NMC811 and LLZO; and (d) NCA and LLZO. The solid triangles (upward facing) indicate the positions of the reflections corresponding to a rock salt structure, NiO in this case (ICSD no. 9866). The open triangles (downward facing) indicate the positions of the reflections corresponding to $LaCoO_3$, a perovskite phase (ICSD no. 17668). The diamonds represent the diffraction pattern of $La_2M_{0.5}Li_{0.5}O_4$ [(M = Ni, Co, Mn, and Al), here from ICSD no. 202439]. The bars at the bottom show the Bragg reflection positions of LLZO and NMC, obtained from the measurements of the pure powders without heat treatment. The reflection positions match those of ICSD 239663 (LLZO) and ICSD 171750 (NMC).

0.5 to 2 h proved to be suitable for establishing proper electrolyte—CAM interfaces. ^{10,11} Initially, the following temperatures were applied: 600, 800, 1000, and 1200 °C. This temperature range was chosen with regard to the overall aim of processing in the context of oxide-based all solid-state batteries, which is governed by two aspects: (i) the temperature should be high enough for sufficient solidification and compaction of the cathode on the one hand, and (ii) the temperature should not exceed the threshold above which significant chemical interaction between the electrolyte and the cathode material occurs, which would result in severe degradation, on the other. Since the phase changes were particularly noticeable when the temperature was increased from 1000 to 1200 °C, additional batches of pressed pellets were heat-treated at 1100 °C.

SEM and EDS were performed on mechanically polished cross sections of the heat-treated samples, which were sputter-coated with a thin platinum layer (several nanometers), by employing a Zeiss Gemini 450 SEM (Carl Zeiss NTS GmbH) device equipped with an Ultim Max 170 EDS detector (Oxford Instruments). A beam accelerating voltage of 16 kV was used. Lithium cannot be detected in such an EDS system, and therefore, correction factors during quantitative EDS analysis would be calculated incorrectly. Moreover, the samples were not measured (calibrated) against known standards (like LLZO with a perfect stoichiometric composition). Both factors may reduce the accuracy of the quantitative EDS results. This fact was taken into consideration when discussing the EDS data in the Results and Discussion section. XRD data were obtained with a Bruker D4 Endeavor (Bruker AXS GmbH) instrument employing Cu Kα radiation. To prepare the samples for the X-ray analysis, the heattreated pellets were ground, and the obtained powder was spread evenly onto double-sided adhesive tape attached to a stainless-steel

sample holder. The raw data were processed and analyzed by utilizing the Rietveld refinement method. The Rietveld analysis was performed with the following parameters as refinable parameters; background, sample displacement, peak profile using fundamental parameters (i.e., size and strain), lattice parameters, and the scale factors of each crystalline phases. The biso value was set to 0.1 for all of the crystalline phases for the quantification. The elemental composition of each sample was assessed by optical emission spectrometry with inductively coupled plasma (ICP-OES), employing an iCAP7600 spectrometer (Thermo Scientific). Prior to the spectroscopy measurements, the heat-treated pellets were ground in a boron carbide mortar, and 50 mg of each sample was subsequently melted with sodium borate at 1050 $^{\circ}\text{C}$ for 30 min. The melt was dissolved in 30 mL of hydrochloric acid (5% concentration). Raman spectra were obtained by employing a Renishaw InVia Raman Microscope equipped with a solid-state excitation laser (532 nm) and a grating of 2400 lines per mm. The measured area was 60 μ m by 40 μ m with a step size of 0.22 μ m. The laser power was set to 2.5 mW to prevent laser-induced sample damage. A total of 49,051 spectra were obtained per sample, with an acquisition time of 1 s per spectrum. The cosmic rays of the raw data were removed by applying Wire 5.2 software (Renishaw). The spectra were truncated to the range from 80 to 1200 cm⁻¹, the background signal was subtracted, and the spectra were normalized by an in-house developed PYTHON script. A non-negative matrix factorization algorithm was chosen to detect the main components of the samples. A selection of 10 compounds yielded the most reasonable results. The compounds were divided into four groups, i.e., LLZO, NMC, secondary phases, and noise. After noise was excluded, the loadings for each group were added up, and for each point in the mapping, only the phase with the highest loading was

considered. Therefore, each point of the spectrum was assigned to either LLZO, NMC, or secondary phases. Finally, the spectra in each group were averaged. Through this analysis, it was possible to extract average spectra for LLZO, NMC, and secondary phases.

RESULTS AND DISCUSSION

XRD Analysis. The temperature stability of LLZO and different CAM compositions was investigated by XRD. The CAM compositions studied included ${\rm LiNi_{1/3}Mn_{1/3}Co_{1/3}O_2}$ (NMC111), ${\rm LiNi_{0.6}Mn_{0.2}Co_{0.2}O_2}$ (NMC622), ${\rm Li-Ni_{0.8}Mn_{0.1}Co_{0.1}O_2}$ (NMC811), and ${\rm LiNi_{0.8}Co_{0.15}Al_{0.05}O_2}$ (NCA).

The combination of NMC111 and LLZO (Figure 1a) appears to be stable at temperatures up to about 1000 °C since NMC111 and LLZO remain as the main phases after cosintering. In the samples sintered at 800 °C and higher, a small fraction (less than 2 wt % according to a Rietveld refinement) of the secondary phase is detected, which can be assigned to La₂M_{0.5}Li_{0.5}O₄ (M = Ni, Co, Mn, and Al) (see, for example, reflection around 31.7° 2 θ angle). In view of the lattice parameters, it seems likely that the main transition metal is Ni. Such a phase was also described in a study on the formation of garnet thin films by sol—gel processing and rapid thermal processing.³⁴

At 1100 °C, an additional minor phase is detected, which can be assigned to about 2 to 4 wt % of a LaMO₃ perovskite phase (M = Ni, Co, and Mn) after Rietveld refinement (Figure 1a). This phase was previously shown to be a reaction product of LLZO with LiCoO₂, where LaCoO₃ was formed. The reference pattern for LaCoO3 agrees quite well with the measured positions, but all reflections are shifted to higher 2θ angles. According to the Bragg equation, this means that the lattice parameters of pure LaCoO3 are too small to adequately describe the experimental results. Other perovskite phases with only one transition metal, such as LaMnO3 and LaNiO3, have larger lattice parameters, mainly due to the larger ionic radii of Mn and Ni in six-fold coordination: Co³⁺: 0.0545 (low spin), 0.061 (high spin); Mn³⁺: 0.058 (low spin), 0.0645 (high spin); and Ni³⁺: 0.056 (low spin), 0.060 (high spin). In a conventional perovskite structure, Mn3+ is in its high spin configuration and Co3+ is in the intermediate spin state, while the configuration of Ni³⁺ in LaNiO₃ is more complex and cannot be described as 3d⁷. According to the ICSD database, LaNiO₃ (ICSD no. 67717) has lattice parameters of a = 5.46 Åand c = 13.15 Å with a $R\overline{3}c$ space group symmetry, LaCoO₃ (ICSD no. 17668) has a = 5.44 Å and c = 13.09 Å, and LaMnO₃ (ICSD no. 96038) has a = 5.50 Å and c = 13.27 Å. The experimental data are best interpreted using a mixed composition with a = 5.483(3) Å and c = 13.20(1) Å. Since three ions with different radii are considered here, there is some arbitrariness in determining the exact composition of the perovskite based on the measured data, which was also discussed in the literature.²¹ Moreover, it is well-known that lattice mismatch, i.e., a deviation of ionic bond lengths compared to an ideal perovskite structure can lead to a change in spin states,³⁵ which complicates a reasonable and reliable calculation of composition. Finally, covalent contributions to the transition metal-oxygen bond and a change in the valence of the ions, e.g., Mn^{4+} (0.053 nm) or Ni $^{2+}$ (0.069 nm), cannot be excluded a priori (all ionic radii were taken from ref 37). Such a valence change was also discussed in.²¹ In summary, the exact composition of the perovskite phase is not clear from the XRD measurements, but the formation of a Co- and Mncontaining secondary phase during cosintering of NMC and LLZO, similar to $LaCo_{1-x}Mn_xO_3$ (x < 0.4) described by Ren et al. is very likely. ^{21,26} Other possible reaction products are single metal oxides, e.g., CoO or NiO, with a rock salt structure. ^{13,21} The peak positions for NiO as an example are also shown in Figure 1a.

When the temperature was increased to 1200 °C, the crystalline phases described above were apparently further altered until a severe decomposition of the original constituents was observed.

The results obtained for Ni-enriched NMC622 are similar to those of NMC111 (Figure 1b). LLZO and NMC622 remain the main phases at temperatures up to 1000 °C, while the secondary phases $\rm La_2M_{0.5}Li_{0.5}O_4$ and perovskite phase amount to less than 2 wt %, according to a Rietveld analysis. Similar to NMC111, strong decomposition occurred at 1200 °C, with the perovskite phase forming as one of the predominant secondary phases. However, in this case, the CAM decomposed strongly in contrast to the results of the tests with NMC111. In addition, LLZO remains present and decomposed to a much lesser extent. Interestingly, the XRD pattern at 1200 °C (Figure 1a) does not contain any clearly discernible peaks for a NiO rock salt phase, in contrast to what was observed for the mixture containing NMC111.

An even stronger decomposition becomes evident when NMC811 with the highest Ni content is cosintered with LLZO under otherwise identical conditions (Figure 1c). On the one hand, the reaction to La₂M_{0.5}Li_{0.5}O₄ at a certain temperature is much more pronounced. On the other hand, the perovskite phase (the predominant secondary phase formed during the decomposition of the LLZO-NMC111 and LLZO-NMC622 mixture) was no longer detected when LLZO-NMC811 was examined. While NMC111 and NMC622 appear to be quite stable up to a temperature of 1100 °C, the intensity of the NMC811 reflections decreased significantly with an increasing heat treatment temperature. At 1100 °C, some wt % of the phase composition was attributed to La₂M_{0.5}Li_{0.5}O₄, while a rock salt phase accounted for about 10 to 15 wt % (fitted with a nominal composition of Li_{0.4}Ni_{1.6}O₂, ICSD no. 71422), as estimated by Rietveld analysis. Figure 1c contains the reflection positions for nominal NiO for comparison, and here, it is even clearer than that in the diffraction patterns obtained with NMC111 and NMC622 that the formation of single metal oxides such as NiO cannot be detected from the experimental

In addition to NMC, the high-temperature reactivity of the manganese-free NCA and LLZO was also investigated (Figure 1d). The formation of secondary phases observed for NMC111, NMC622, and NMC811 can be clearly applied to NCA: the reaction that yields La₂M_{0.5}Li_{0.5}O₄ was even more pronounced compared to LLZO-NMC811 in the lower temperature range studied in this work. The perovskite phase, which was found for LLZO-NMC111 and LLZO-NMC622 and was absent for LLZO-NMC811, cannot be detected in LLZO-NCA either. In addition, more than half of the NCA decomposed at 1100 °C, about 4 to 6 wt % of La₂M_{0.5}Li_{0.5}O₄ formed, and about 25 to 30% (compared to 10 to 20 wt % for NMC811) of all observed phases can be assigned to the rock salt phase, as assessed by Rietveld refinement.

A graphical summary of the XRD analysis results for all CAM compositions studied is shown in Figure 2 for a better illustration of the development of the phases. In general, CAM

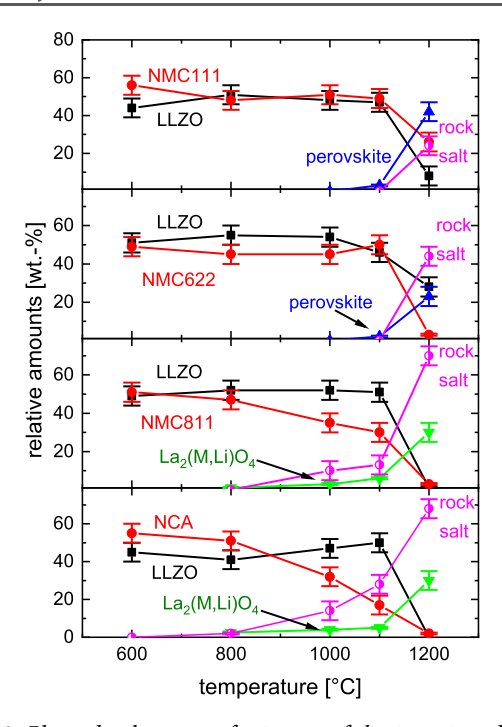


Figure 2. Phase development of mixtures of the investigated CAMs and LLZO as a function of temperature. The exact compositions of the respective phases that were formed as a result of the decomposition reactions are not known. Therefore, certain phases, which were considered to be most plausible, were evaluated [e.g., LaMnO₃, LaNiO₃, and LaCoO₃ to represent a La(Mn,Ni,Co)O₃ phase], and the deviations in the relative amounts were the basis for the error bars in the plots. La₂(M,Li)O₄ was within the error bars detected only for NMC811 and NCA.

and LLZO are the predominant phases for all CAM compositions at temperatures up to 1000 °C. Only small amounts of secondary phases were formed below 1000 °C, and greater decomposition of NMC and LLZO was observed at 1100 and 1200 °C. Figure 2 illustrates, as a trend, that NMC811 and NCA are more reactive than NMC111 and NMC622. The obtained findings are consistent with the results of the previously published in situ high-temperature XRD experiments, where the LaCo_{1-x}Mn_xO₃ perovskite phase was observed and La₂Ni_{0.5}Li_{0.5}O₄ was identified as a La₂M_{0.5}Li_{0.5}O₄ equivalent phase in conjunction with NMC111 at a temperature of 800 °C and above. 26

In Roitzheim et al., 26 La₂Ni_{0.5}Li_{0.5}O₄ has been found as the dominating phase detected by XRD in the case of NMC811 in the temperature regime between 650 and 1000 °C, attributed to the different heat treatment procedure and data acquisition. These findings were obtained by adjusting the temperature in 50 °C increments using a ramp rate of 5 K/min with a holding time of approximately 37 min during the diffraction measurement. Furthermore, the data were only collected from the surface of the NMC/LLZO pellets. 26

In this work, the pellets were sintered at discrete temperatures in a closed crucible, with a compacted powder bed that was composed of LLZO and CAM underneath the pellet (see the Experimental Part section). Thus, differences with respect to the onset temperature of certain types of secondary phase formation seem plausible (like different Li evaporation or ion diffusion behavior).

The mixture of NMC111 and LLZO remained in a rather stable state at temperatures of up to 1000 °C. After heat

treatment at 1200 °C, perovskite phases clearly developed, and to a lesser extent, a rock salt phase was also observed. Similarly, NMC622 appeared to be stable and decomposed to a lesser extent into a perovskite phase and also a rock salt phase compared to NMC111. For NMC811 and LLZO, the CAM decomposed at a lower temperature, and a La₂(M, Li)O₄ phase (M = Ni, Mn, Co) rather than a perovskite phase was formed. The formation of the rock salt phase was the most pronounced. With respect to NCA, similar observations were made as for NMC811.

In the previous sections, a systematic temperature-dependent evolution of the crystal phases of LLZO-NMC and LLZO-NCA mixtures was discussed, starting from a high Mn content to a CAM without Mn. Three La-containing secondary phases were identified during cosintering of LLZO and different CAMs, but Li₂MnO₃ and La₂Zr₂O₇, both typical reaction products of LLZO with high voltage CAM, ¹³ were not detected, and the same is true for CoO(OH) (neither as the P6₃/mmc nor the R3m space group). Li₂ZrO₃, another commonly observed phase, was also not detected. One should note that Li₂ZrO₃ can react rapidly with CO₂

$$\text{Li}_2\text{ZrO}_3 + \text{CO}_2 \rightarrow \text{ZrO}_2 + \text{Li}_2\text{CO}_3$$
 (1)

This reaction could result in a core—shell structure with a $\rm Li_2ZrO_3$ core covered by a $\rm ZrO_2$ surface layer and an overlying $\rm Li_2CO_3$ layer. ³⁸ It is plausible that $\rm Li_2ZrO_3$ might not be visible due to a screening effect caused by these outer layers. $\rm Co_3O_4$ was not observed by XRD, although it has been reported as a reaction product for LLZO—spinel mixtures. ¹³

Two major problems arise from the XRD analysis that necessarily require a thorough review of the results discussed above. The XRD patterns clearly contain signals corresponding to a rock salt and a spinel phase. However, when metal monoxides such as NiO and perovskites such LaMnO₃ are chosen as reaction products with rock salt and spinel phase, respectively, in the Rietveld refinement, there appears to be no Zr-containing reaction product even when the signals from LLZO disappear completely from the XRD pattern (1200 °C). In addition, although the decomposition products containing transition metals of NMC and La appear to track properly, the peak positions matched the reference positions reasonably well but not perfectly.

Chemical element analysis (ICP-OES) showed no evidence of a systematic change in the cation content (including Zr) as a result of heat treatment except for an apparent loss of lithium. The latter could be due to the formation and evaporation of LiOH (melting point 473 °C³⁹) or Li₂CO₃ (melting point between 714 and 733 °C⁴⁰). Thus, Zr-containing crystalline phases must be present in the sample. The formation of amorphous phases is unlikely since no diffuse reflection at low angles indicating amorphous phases was observed in the XRD patterns.

A possible explanation for these discrepancies and inaccuracies is the incorrect assignment of reaction products. Based on theoretical considerations followed by experimental verification, Urban et al. presented another phase with composition Li_{0.5}Co_{0.25}Zr_{0.25}O, which is very similar to a rock salt phase like CoO.⁴¹ Cambaz et al. published the observation of a rock salt phase LiNi_{0.5}Zr_{0.5}O₂, ⁴² and Li et al. presented a LiMn_{0.5}Zr_{0.5}O₂ rock salt phase¹⁸ in their work. This type of phase was used to fit the diffraction patterns of the samples sintered at 1200 °C in our work (Figure 3). While a refinement involving a NiO phase yields reasonable results, an

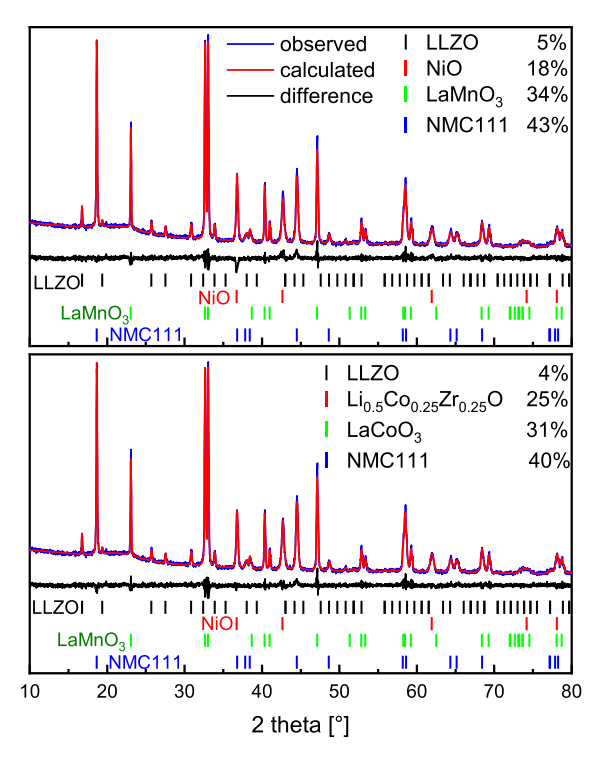


Figure 3. Top: Rietveld refinement of a mixture of LLZO and NMC111 after heat treatment at 1200 °C, i.e., in the severe decomposition range, based on simple transition-metal-based oxides ($R_{\rm wp} \approx 3.19\%$). The percentages next to the listed compounds represent the nominal weight ratios. Bottom: refinement after introducing the novel phase Li_{0.5}Co_{0.25}Zr_{0.25}O in addition to the transition-metal-based oxides ($R_{\rm wp} \approx 2.86\%$) (see Urban et al. ⁴¹ for details to the crystal structure of Li_{0.5}Co_{0.25}Zr_{0.25}O. The corresponding ICSD numbers of the other phases can be found in the text).

obviously even better fit could be obtained if a $\text{Li}_{0.5}\text{Co}_{0.25}\text{Zr}_{0.25}\text{O}_2$ phase was used for the refinement. These results clearly indicate that great care must be taken in selecting potentially suitable crystal phases for Rietveld refinement. It is possible that previous publications underestimated the importance of such rather unconventional phases.

A small and broad elevation of the XRD signal between ca. 20 and 25° 2θ is detectable. It is supposed that this is a background artifact due to the setup. Also the Rietveld refinement did not give rise to any assumption that a phase were overlooked. More details to the Rietveld refinement can be found in the Supporting Information.

The determination of a possible composition of the perovskite phase is further complicated by the fact that, in addition to Ni, Co, and Mn, Zr^{4+} ions can also substitute transition-metal ion sites in a perovskite structure. A The ionic radius of Zr^{4+} in six-fold coordination is 0.072 nm. Pure stoichiometric $LaZrO_3$ as a reaction product with the perovskite structure would be possible with regard to the ionic radii and the Goldschmidt tolerance factor Zr^{3-3} , but can be

excluded because either La or Zr ions would not be in their stable oxidation state in this phase. A perovskite structure is possible with Ca²⁺, which has a similar ionic radius to La³⁺ in 12-fold coordination, although literature values for the lattice parameters differ considerably, e.g., $a = 4.01 \text{ Å in}^{46} \text{ vs } a = 5.59$ Å in.⁴⁷ Alternatively, La-site deficient perovskites La_{2/3}ZrO₃ as published in 48,49 may be taken into consideration, where nominal charge neutrality is given. With view to ionic radii, also Li and Ta ions with six-fold coordination would fit into the perovskite lattice. As examples, Thangadurai et al.⁵⁰ and Huang et al.⁵¹ published novel Li-containing perovskite materials with sophisticated compositions with rational number stoichiometry, while Yokokawa et al.⁵² and Vieten et al.⁵³ pointed out the stability limits of perovskites with ions with different ionic radii on the respective perovskite lattice sites. These issues make the calculation of the perovskite composition based on XRD data and ionic radii alone even less accurate.

Finally, Zr^{4+} ions can also be incorporated into the NMC crystal. An incorporation of 5 at. % Zr into the LiNi_{0.8}Co_{0.2}O₂ lattice without compromising the crystal structure has been published.⁵⁴ Lipson et al.⁵⁵ and Liu et al.⁵⁶ demonstrated XRD peak shifts to smaller angles, i.e., an increase in lattice parameters, for NMC622 by partial Zr ion substitution.

It is known that NMC materials lose oxygen during thermal treatment, and there is experimental evidence that oxygen loss in NMC can also lead to enlarged lattice parameters. The extent to which oxygen can be reintegrated into the crystal lattice appears to depend on the cooling rate. At this stage, it cannot be ruled out that the NMC/NCA samples used in this work are also subjected to some oxygen loss during heating and subsequent cooling, which would also affect the lattice parameter.

In summary, Zr⁴⁺ ions can diffuse into the rock salt, perovskite, and NMC or NCA crystal lattice, which explains the lack of distinct Zr-containing phases in the XRD patterns. This possibility is supported by SEM investigations, which are discussed in more detail in the next section.

SEM Analysis. The contrast observed in backscattered electron (BSE) images in SEM depends on the atomic number (so-called Z contrast). Table 1 contains the nominal mean atomic numbers of the phases assigned in the XRD analysis, calculated according to the formulas in Howell et al. and Love et al. S9,60 Since the accuracy of Z contrast determination in the BSE mode is not very high and the differences of $\Delta Z = \pm 2$ are indistinguishable, the NMC compositions and the Li_{0.5}Co_{0.25}Zr_{0.25}O rock salt phase in Table 1 would show very similar contrast in BSE images.

Phases with a high relative La content, i.e., $La_2Ni_{0.5}Li_{0.5}O_4$, have the highest average atomic numbers, followed by the perovskite-type compositions. Metal monoxides and LLZO have intermediate values, and NMC compounds have the lowest values of averaged atomic numbers. Interestingly, the averaged atomic number of the $Li_{0.5}Co_{0.25}Zr_{0.25}O$ rock salt phase discussed above is very close to that of NMC. Therefore,

Table 1. Calculated Mean Atomic Numbers of Compounds Discussed in the XRD Section

| $Li_{6.45}Al_{0.05}La_3Zr_{1.6}Ta_{0.4}O_{12}$ | NMC111 | NMC622 | NMC811 | NiO | CoO |
|---|---------------------------|---------------------------|-----------|-----------|-----------|
| 16.2 | 11.4 | 11.6 | 11.7 | 18.0 | 17.5 |
| $\text{Li}_{0.5}\text{Co}_{0.25}\text{Zr}_{0.25}\text{O}$ | $La_2Ni_{0.5}Li_{0.5}O_4$ | Li_2ZrO_3 | $LaMnO_3$ | $LaCoO_3$ | Co_3O_4 |
| 13.1 | 23.1 | 11.7 | 21.2 | 21.6 | 16.1 |

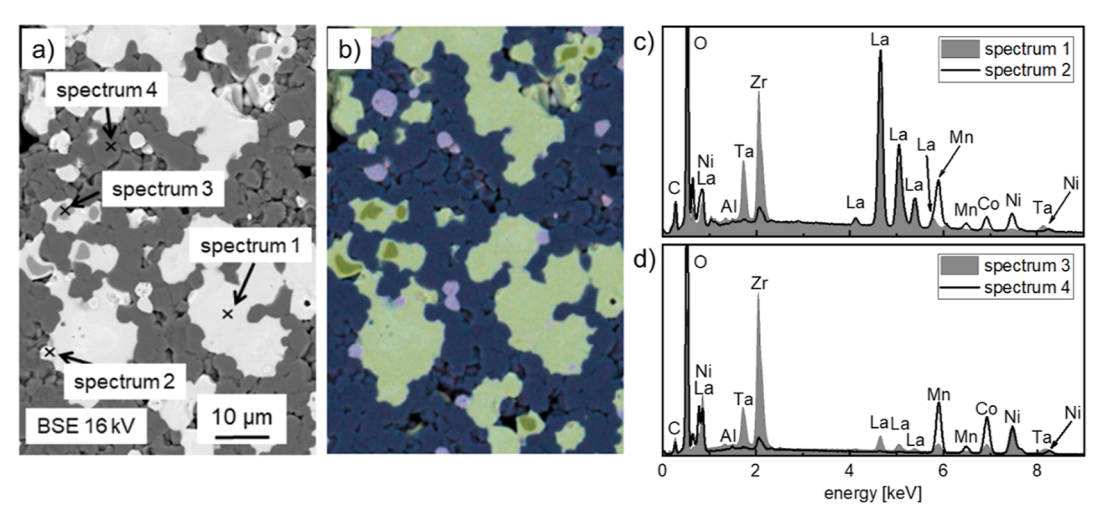


Figure 4. (a) BSE image of a mixture of LLZO-NMC111 sintered at 1100 °C and (b) layered image of the single EDS mappings of La, O, Zr, Mn, Co, Ni, and Ta. Dark blue areas in this image show mainly the NMC111, and bright green areas show the LLZO. Dark green and violet show newly formed phases (see text). Graphics: EDS spectra of regions 1 and 2 (c) and regions 3 and 4 (d).

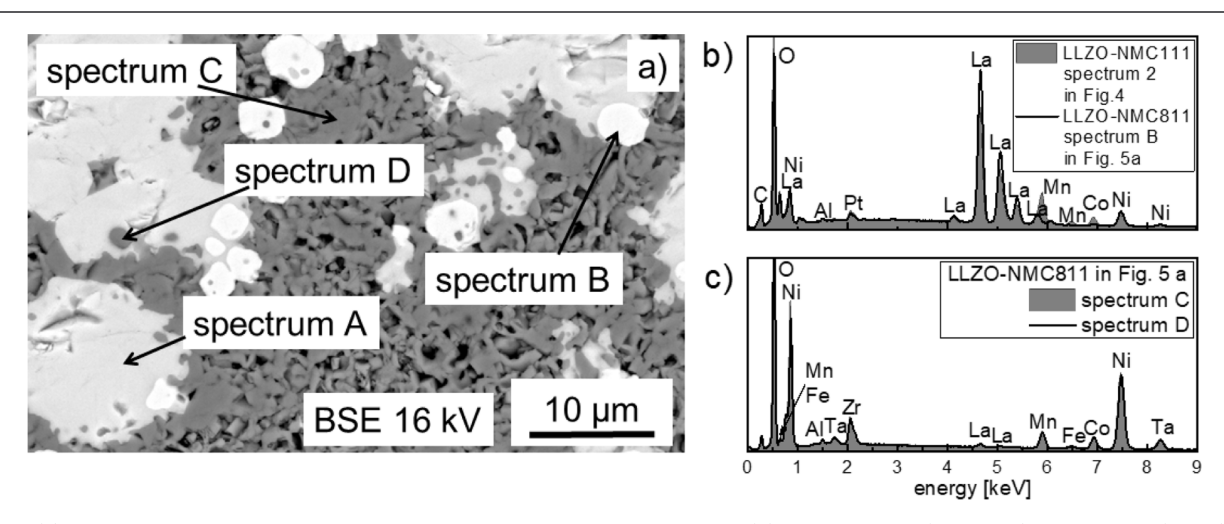


Figure 5. (a) BSE image of a mixture of LLZO and NMC811, heat-treated at 1100 °C; (b) EDS spectra B (NMC811) of this figure (part a) and 2 (NMC111) (of Figure 4), indicating that the bright phase has a higher ratio of La to transition metals than that in the case of NMC111; and (c) EDS spectra of the dark gray areas (spectrum C and spectrum D), showing that both dark phases have a very similar composition and both contain Zr as well as Ta.

only a minor difference in contrast between NMC and the $\text{Li}_{0.5}\text{M}_{0.25}\text{Zr}_{0.25}\text{O}$ rock salt phase is expected in BSE images. NMC compounds containing a certain amount of Zr have an average Z number between pure NMC and the rock salt phase.

Figure 4a shows an SEM image of LLZO-NMC111 sintered at 1100 °C taken with BSEs (i.e., the Z contrast is particularly visible), along with a layered image derived from EDS mappings Figure 4b. Four different regions with different contrasts and compositions can be clearly distinguished.

Spectrum 1 taken in the large light gray region ("region 1") contains O, Al, Ta, La, and Zr and can be assigned to LLZO, in agreement with the XRD data (Figures 1 and 3). The ratio of Zr and Ta derived from EDS agrees very well with the nominal ratio in LLZO. However, there is obvious deficiency of about 20 at. % with respect to La. Another distinct phase with an even brighter gray scale was found (area with spectrum 2, "region 2"). It consists mainly of La, Mn, Ni, and Co and contains much less Zr and Ta compared to the region 1. Considering the XRD results and the brightness of the BSE image, region 2 appears to be La₂ $M_{0.5}$ Li_{0.5}O₄ (M = Ni, Co, and

Mn; Li cannot be detected by the EDS detector) or LaMO₃ (M = Ni, Co, Mn, and Zr). According to the EDS-based quantification of the cations, the ratio of La to the sum of transition metals is very close to 1:1, indicating the formation of the LaMO₃ phase and not La₂M_{0.5}Li_{0.5}O₄. In addition, it appears to be a Mn-rich perovskite. It should be noted that the EDS could overlap with the EDS signal from Pt, resulting in what appears to be apparently increased Zr peak as an artifact (L α line of Zr: 2.0424 eV; M α line of Pt: 2.0485 eV; see also the EDS spectra in Figure 5 where Pt was identified instead of Zr; thus, small amounts of Zr could be concealed by the EDS signal from Pt). It cannot be excluded that the excitation volume of the phase with high atomic numbers is increased to such a degree that signals from the original LLZO material can also be detected.

Spectrum 4 taken in the large dark gray region ("region 4") contains mainly Ni, Mn, and Co in a ratio close to Ni/Mn/Co = 1:1:1 (while other cations appear to contribute less than 1 at. %), which agrees well with the NMC111 composition. In addition to region 4, much smaller areas with light gray

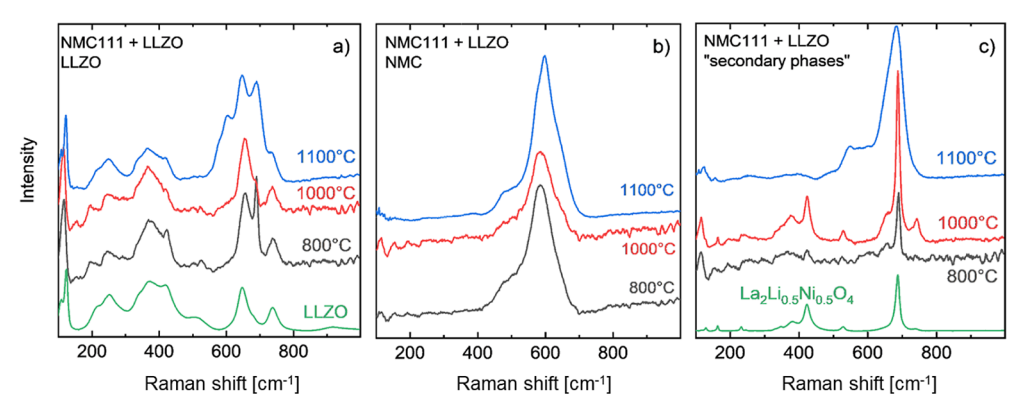


Figure 6. Raman spectra of LLZO, NMC111, and secondary phases in mixtures of NMC111 and LLZO heat-treated at 800, 1000, and 1100 $^{\circ}$ C. A Raman spectrum obtained with pure LLZO was added [(a) green] for comparison. The Raman peaks associated with NMC111 indicate that the NMC111 phase is mainly conserved during heat treatment (b). Pure La₂Li_{0.5}Ni_{0.5}O₄ was synthesized in-house to provide a suitable reference measurement [(c) green color].

contrast have also been detected in BSE images [spectrum 3, "region(s) 3"]. The EDS spectrum of these regions shows a strong signal of Zr as a major element, and apparently the same content of Ni as in NMC but with smaller amounts of Co and Mn compared to NMC. The ratio of Zr to the sum of Mn, Co, and Ni is close to 1:1, which agrees well with the composition of $\text{Li}_{0.5}\text{M}_{0.25}\text{Zr}_{0.25}\text{O}$ (M = Ni, Co, Mn, and Zr) rock salt phase discussed above. Moreover, signals corresponding to Ta (however, only half of the nominal content of LLZO) and La are visible but much smaller than that in LLZO when considering the intensity of the Zr peak in the same spectrum. Regions 3 always appear close to or apparently even within the LLZO particles. It is possible that EDS signals from the surrounding areas were partly detected, as well.

The SEM analysis described above was also performed for the mixture of LLZO and NMC811 heated to 1100 °C (Figure 5). Two light gray areas are also visible in this composition: the large bright region A associated (associated with spectrum A) can be assigned to LLZO (based on the EDS analysis), as for the LLZO-NMC111 mixture. In addition, another region B with even brighter contrast than LLZO and thus a much higher average Z value was detected (spectrum B). EDS quantification shows that the composition of this very bright region differs significantly from region 2 in the LLZO-NMC811 mixture as it contains more La and fewer transition metals (Figure 5; Figure 5c spectra 2 and B). Ni is the predominant transition metal, while the amount of Mn and Co is lower by 1 order of magnitude. Moreover, the La/Ni molar ratio is about 3.8, which, in contrast to the findings of NMC111, indicates the formation of La₂Ni_{0.5}Li_{0.5}O₄ rather than a perovskite phase. The observation of this phase agrees well with our earlier publication, in which the formation of isolated light gray particles of La₂Ni_{0.5}Li_{0.5}O₄ was observed after sintering at 800 °C.²⁶ A similar morphology seems to be preserved even at the much higher temperature of 1100 °C used in this work.

Similar to NMC111, the formation of dark gray regions within the LLZO particles is also observed for the NMC811 (region D, with spectrum D). However, there are major differences in the chemical compositions of these regions in the two NMC compositions. For NMC111, these regions contain a high amount of Zr and were assigned to a rock salt phase (Figure 4). However, the composition of these domains for the LLZO-NMC811 mixture is very similar to that of the pure NMC811 grains (Figure 5c, region C, with spectrum C), (with Ni/Mn/Co \approx 8:0.9:1 according to EDS measurements).

Interestingly, and in contrast to NMC111, a significant fraction of Zr is found in this region, i.e., $Zr/Co \approx 0.6:1$. Therefore, we interpret our results to mean that NMC811 serves as a host for Zr.

Intriguingly, no evidence of a rock salt phase was found in our SEM analysis, although such a phase was originally identified in LLZO-NMC811 mixtures by Rietveld refinement. The reason for this remains unclear at this stage.

SEM and EDS analyses show that after cosintering of NMC111 and LLZO at 1200 $^{\circ}$ C, a Mn-rich perovskite as well as a Zr-containing rock salt phase (Li_{0.5}M_{0.25}Zr_{0.25}O; M = Ni, Co, and Mn) are formed, while only La₂Ni_{0.5}Li_{0.5}O₄ forms as a secondary phase, and Zr is incorporated into the NMC811 host structure when NMC811 and LLZO are cosintered at the same temperature.

Raman Spectroscopy Analysis. Figure 6 shows the Raman spectra of the LLZO-NMC111 mixtures heated at 800, 1000, and 1100 °C, respectively. The three plots show the data assigned to LLZO, NMC111, and the secondary phases determined by an extraction algorithm, as described in the Experimental Part. LLZO and NMC111 appear to be quite stable in this temperature range, as confirmed by the XRD analysis (Figure 6a,b). The Raman spectrum of a secondary phase formed after heating at 800 and 1000 °C is very similar to that of $\text{La}_2\text{Li}_{0.5}\text{Ni}_{0.5}\text{O}_4$. However, a phase change occurs at higher temperatures, and the spectrum of the phase formed at 1100 °C agrees quite well with a Raman spectrum reported for perovskites. This is also consistent with the results of the XRD analysis.

In addition to the Raman spectrum of pure LLZO, an additional peak is observed that is consistent with the spectrum of $La_2Li_{0.5}M_{0.5}O_4$ (Figure 6a). Presumably, in addition to the main phases, a fraction of $La_2Li_{0.5}M_{0.5}O_4$ is also present in the regions composed predominantly of LLZO.

CONCLUSIONS

When mixtures of LLZO and different NMC compositions such as NMC111, NMC622, NMC811, and NCA were sintered together at temperature ranging from 800 to 1100 $^{\circ}$ C, the initial CAM and LLZO phases were mainly preserved. However, various secondary phases were observed, the nature and amount of which were influenced by the chemical composition of the NMC. In general, three secondary phases were identified, namely, La₂Li_{0.5}M_{0.5}O₄ (M = Ni, Co, and Mn),

a perovskite phase LaMO₃ (M = Ni, Co, and Mn), and a $\text{Li}_{0.5}\text{M}_{0.25}\text{Zr}_{0.25}\text{O}$ (M = Ni, Co, and Mn) rock salt phase. The temperature of the reaction onset depends strongly on the active cathode materials used. For all NMC compositions, $\text{La}_2\text{Li}_{0.5}\text{M}_{0.5}\text{O}_4$ (M = Ni, Co, and Mn) forms at 800 °C and above. In the case of NMC111 and NMC622, the perovskite phase appears as a major phase after cosintering at higher temperatures (1000 °C and above). In the case of NMC811 and NCA, this perovskite phase apparently does not form at all. The rock salt phase also forms at 1000 °C and above for NMC111 and NMC622, but it forms already at 800 and 600 °C for NMC811 and NCA, respectively.

For all mixtures of LLZO and the CAMs studied, the relative amount of secondary phases increases at higher temperatures. In general, it can be observed that the reactivity of the different NMC compositions toward LLZO during cosintering increases with increasing Ni content (measured by the amount of secondary phases in the XRD analysis as a function of temperature). However, in addition to the type and concentration of secondary phases formed at a given temperature, their electrochemical properties should also be considered to identify suitable cathodes for garnet-type all solid-state batteries. The electrochemical properties of the secondary phases observed in this study have not yet been investigated, and no data could be found for pure La₂Li_{0.5}M_{0.5}O₄, for the rock salt-type LiM_{0.5}Zr_{0.5}O₂, or the perovskite LaMO₃ phases.

Our study shows that a comprehensive analysis of different characterization techniques is necessary to correctly identify the incidents occurring during the sintering of mixtures of CAM and garnet-based electrolytes. Our investigations revealed the formation of two important secondary phases not considered in previous analyses, namely, rock salt phases of the $\text{LiM}_{0.5}\text{Zr}_{0.5}\text{O}_2$ type (M = Ni, Mn, and Co) and NMC-like structures with significant partial replacement of transition metals by zirconium.

Similar reactions were observed for the CAM LiCoO₂ in conjunction with LLZO during conventional sintering. ¹¹ An approach of liquid phase sintering appears questionable with view to publications on processing with liquid precursors which rather promoted than inhibited the detrimental reactions. ¹¹ Another way that has been intensively investigated was the application of coatings between CAMs and solid electrolyte, see ²⁴ and references therein, it recently turned out that reducing the interaction time at high temperature is a significantly more promising strategy, for example, rapid thermal processing, ⁶³ ultrafast high-temperature sintering, ⁶⁴ or laser sintering. ⁶⁵ Therefore, it is self-evident to transfer this approach to the processing of composite cathodes containing NMC materials.

ASSOCIATED CONTENT

Supporting Information

The Supporting Information is available free of charge at https://pubs.acs.org/doi/10.1021/acs.chemmater.3c01573.

Rietveld refinement results for $\text{Li}_{0.5-0.5x}M_{0.25+0.75x}\text{Zr}_{0.25-0.25x}\text{O}$ (M = Co and Ni) (PDF)

AUTHOR INFORMATION

Corresponding Author

Sven Uhlenbruck — Institute of Energy and Climate Research, Materials Synthesis and Processing (IEK-1), Forschungszentrum Jülich GmbH, 52425 Jülich, Germany; Helmholtz Institute Münster: Ionics in Energy Storage (IEK-12), Forschungszentrum Jülich GmbH, 48149 Münster, Germany; orcid.org/0000-0003-0334-0425; Email: s.uhlenbruck@fz-juelich.de

Authors

Alexander Bauer – Institute of Energy and Climate Research, Materials Synthesis and Processing (IEK-1) and Institute of Energy and Climate Research, Fundamental Electrochemistry (IEK-9), Forschungszentrum Jülich GmbH, 52425 Jülich, Germany

Christoph Roitzheim — Institute of Energy and Climate Research, Materials Synthesis and Processing (IEK-1), Forschungszentrum Jülich GmbH, 52425 Jülich, Germany; orcid.org/0000-0001-8757-9868

Sandra Lobe – Institute of Energy and Climate Research, Materials Synthesis and Processing (IEK-1), Forschungszentrum Jülich GmbH, 52425 Jülich, Germany

Yoo Jung Sohn — Institute of Energy and Climate Research, Materials Synthesis and Processing (IEK-1), Forschungszentrum Jülich GmbH, 52425 Jülich, Germany; orcid.org/0000-0002-7994-7269

Doris Sebold – Institute of Energy and Climate Research, Materials Synthesis and Processing (IEK-1), Forschungszentrum Jülich GmbH, 52425 Jülich, Germany

Walter Sebastian Scheld — Institute of Energy and Climate Research, Materials Synthesis and Processing (IEK-1), Forschungszentrum Jülich GmbH, 52425 Jülich, Germany; Faculty of Engineering and Center for Nanointegration Duisburg-Essen (CENIDE), Universität Duisburg-Essen, 47057 Duisburg, Germany

Martin Finsterbusch — Institute of Energy and Climate Research, Materials Synthesis and Processing (IEK-1), Forschungszentrum Jülich GmbH, 52425 Jülich, Germany; Helmholtz Institute Münster: Ionics in Energy Storage (IEK-12), Forschungszentrum Jülich GmbH, 48149 Münster, Germany; orcid.org/0000-0001-7027-7636

Olivier Guillon — Institute of Energy and Climate Research, Materials Synthesis and Processing (IEK-1), Forschungszentrum Jülich GmbH, 52425 Jülich, Germany; Helmholtz Institute Münster: Ionics in Energy Storage (IEK-12), Forschungszentrum Jülich GmbH, 48149 Münster, Germany; Jülich Aachen Research Alliance: JARA-Energy, 52425 Jülich, Germany

Dina Fattakhova-Rohlfing — Institute of Energy and Climate Research, Materials Synthesis and Processing (IEK-1), Forschungszentrum Jülich GmbH, 52425 Jülich, Germany; Helmholtz Institute Münster: Ionics in Energy Storage (IEK-12), Forschungszentrum Jülich GmbH, 48149 Münster, Germany; Faculty of Engineering and Center for Nanointegration Duisburg-Essen (CENIDE), Universität Duisburg-Essen, 47057 Duisburg, Germany; orcid.org/0000-0003-2008-0151

Complete contact information is available at: https://pubs.acs.org/10.1021/acs.chemmater.3c01573

Author Contributions

The manuscript was written through contributions of all authors. All authors have given approval to the final version of the manuscript.

Notes

The authors declare no competing financial interest.

ACKNOWLEDGMENTS

The financial support from the Federal Ministry of Education and Research of Germany through projects 13XP0173A and 13XP0434A (FestBatt/2—Oxide), 03EK3572 (UNIBAT) and 13XP0223A and 13XP0510A (CatSE/2), the Federal Ministry of Economic Affairs and Climate Action of Germany through project no. 03ETE016F (Optikeralyt), and the Helmholtz Association of German Research Centers for their financial support within the Helmholtz program "MTET: Materials and Technologies for the Energy Transition," topic "Electrochemical energy storage" is gratefully acknowledged. The authors thank V. Nischwitz, ZEA-3, Forschungszentrum Jülich, for performing the ICP-OES analyses. The authors are responsible for the content of this work.

REFERENCES

- (1) Murugan, R.; Thangadurai, V.; Weppner, W. Fast Lithium Ion Conduction in Garnet-Type Li7La3Zr2O12. *Angew. Chem., Int. Ed.* **2007**, *46*, 7778–7781.
- (2) Buschmann, H.; Dölle, J.; Berendts, S.; Kuhn, A.; Bottke, P.; Wilkening, M.; Heitjans, P.; Senyshyn, A.; Ehrenberg, H.; Lotnyk, A.; et al. Structure and dynamics of the fast lithium ion conductor "Li7La3Zr2O12". *Phys. Chem. Chem. Phys.* **2011**, *13*, 19378–19392.
- (3) Tsai, C.-L.; Dashjav, E.; Hammer, É.; Finsterbusch, M.; Tietz, F.; Uhlenbruck, S.; Buchkremer, H. High conductivity of mixed phase Alsubstituted Li7La3Zr2O12. *J. Electroceram.* **2015**, *35*, 25–32.
- (4) Tsai, C.-L.; Roddatis, V.; Chandran, C. V.; Ma, Q.; Uhlenbruck, S.; Bram, M.; Heitjans, P.; Guillon, O. Li7La3Zr2O12 Interface Modification for Li Dendrite Prevention. ACS Appl. Mater. Interfaces 2016, 8, 10617–10626.
- (5) Buannic, L.; Orayech, B.; López Del Amo, J. M.; Carrasco, J.; Katcho, N. A.; Aguesse, F.; Manalastas, W.; Zhang, W.; Kilner, J.; Llordés, A. Dual Substitution Strategy to Enhance Li+ Ionic Conductivity in Li7La3Zr2O12 Solid Electrolyte. *Chem. Mater.* **2017**, 29, 1769–1778.
- (6) Xiao, Y.; Wang, Y.; Bo, S.-H.; Kim, J. C.; Miara, L. J.; Ceder, G. Understanding interface stability in solid-state batteries. *Nat. Rev. Mater.* **2020**, *5*, 105–126.
- (7) Ren, Y.; Danner, T.; Moy, A.; Finsterbusch, M.; Hamann, T.; Dippell, J.; Fuchs, T.; Müller, M.; Hoft, R.; Weber, A.; et al. Oxide-Based Solid-State Batteries: A Perspective on Composite Cathode Architecture. *Adv. Energy Mater.* **2022**, *13*, 2201939.
- (8) Demuth, T.; Fuchs, T.; Walther, F.; Pokle, A.; Ahmed, S.; Malaki, M.; Beyer, A.; Janek, J.; Volz, K. Influence of the sintering temperature on LLZO-NCM cathode composites for solid-state batteries studied by transmission electron microscopy. *Matter* **2023**, *6*, 2324–2339.
- (9) Finsterbusch, M.; Danner, T.; Tsai, C.-L.; Uhlenbruck, S.; Latz, A.; Guillon, O. High Capacity Garnet-Based All-Solid-State Lithium Batteries: Fabrication and 3D-Microstructure Resolved Modeling. ACS Appl. Mater. Interfaces 2018, 10, 22329–22339.
- (10) Tsai, C.-L.; Ma, Q.; Dellen, C.; Lobe, S.; Vondahlen, F.; Windmüller, A.; Grüner, D.; Zheng, H.; Uhlenbruck, S.; Finsterbusch, M.; et al. A garnet structure-based all-solid-state Li battery without interface modification: resolving incompatibility issues on positive electrodes. Sustainable Energy Fuels 2019, 3, 280–291.
- (11) Uhlenbruck, S.; Dornseiffer, J.; Lobe, S.; Dellen, C.; Tsai, C.-L.; Gotzen, B.; Sebold, D.; Finsterbusch, M.; Guillon, O. Cathode-

- electrolyte material interactions during manufacturing of inorganic solid-state lithium batteries. *J. Electroceram.* **2017**, *38*, 197–206.
- (12) Scheld, W. S.; Lobe, S.; Uhlenbruck, S.; Dellen, C.; Sohn, Y. J.; Hoff, L. C.; Vondahlen, F.; Guillon, O.; Fattakhova-Rohlfing, D. Rapid thermal sintering of screen-printed LiCoO2 films. *Thin Solid Films* **2022**, 749, 139177.
- (13) Miara, L.; Windmüller, A.; Tsai, C.-L.; Richards, W. D.; Ma, Q.; Uhlenbruck, S.; Guillon, O.; Ceder, G. About the Compatibility between High Voltage Spinel Cathode Materials and Solid Oxide Electrolytes as a Function of Temperature. *ACS Appl. Mater. Interfaces* **2016**, *8*, 26842–26850.
- (14) Bachman, J. C.; Muy, S.; Grimaud, A.; Chang, H.-H.; Pour, N.; Lux, S. F.; Paschos, O.; Maglia, F.; Lupart, S.; Lamp, P.; et al. Inorganic Solid-State Electrolytes for Lithium Batteries: Mechanisms and Properties Governing Ion Conduction. *Chem. Rev.* **2016**, *116*, 140–162.
- (15) Windmüller, A.; Tsai, C.-L.; Möller, S.; Balski, M.; Sohn, Y. J.; Uhlenbruck, S.; Guillon, O. Enhancing the performance of high-voltage LiCoMnO4 spinel electrodes by fluorination. *J. Power Sources* **2017**, *341*, 122–129.
- (16) Windmüller, A.; Bridges, C. A.; Tsai, C.-L.; Lobe, S.; Dellen, C.; Veith, G. M.; Finsterbusch, M.; Uhlenbruck, S.; Guillon, O. Impact of Fluorination on Phase Stability, Crystal Chemistry, and Capacity of LiCoMnO4 High Voltage Spinels. *ACS Appl. Energy Mater.* **2018**, *1*, 715–724.
- (17) Radin, M. D.; Hy, S.; Sina, M.; Fang, C.; Liu, H.; Vinckeviciute, J.; Zhang, M.; Whittingham, M. S.; Meng, Y. S.; Van der Ven, A. Narrowing the Gap between Theoretical and Practical Capacities in Li-Ion Layered Oxide Cathode Materials. *Adv. Energy Mater.* **2017**, *7*, 1602888.
- (18) Li, B.; Wang, Q.; Zhang, Y.; Song, Z.; Yang, D. Nickel-Modified and Zirconium-Modified Li2MnO3 and Applications in Lithium-Ion Battery. *Int. J. Electrochem. Sci.* **2013**, *8*, 5396–5406.
- (19) Minnmann, P.; Quillman, L.; Burkhardt, S.; Richter, F. H.; Janek, J. Editors' Choice-Quantifying the Impact of Charge Transport Bottlenecks in Composite Cathodes of All-Solid-State Batteries. *J. Electrochem. Soc.* **2021**, *168*, 040537.
- (20) Zhang, N.; Long, X.; Wang, Z.; Yu, P.; Han, F.; Fu, J.; Ren, G.; Wu, Y.; Zheng, S.; Huang, W.; et al. Mechanism Study on the Interfacial Stability of a Lithium Garnet-Type Oxide Electrolyte against Cathode Materials. ACS Appl. Energy Mater. 2018, 1, 5968—5976.
- (21) Ren, Y.; Liu, T.; Shen, Y.; Lin, Y.; Nan, C.-W. Chemical compatibility between garnet-like solid state electrolyte Li6.75-La3Zr1.75Ta0.25O12 and major commercial lithium battery cathode materials. *J. Materiomics* **2016**, *2*, 256–264.
- (22) Nie, K.; Hong, Y.; Qiu, J.; Li, Q.; Yu, X.; Li, H.; Chen, L. Interfaces Between Cathode and Electrolyte in Solid State Lithium Batteries: Challenges and Perspectives. *Front. Chem.* **2018**, *6*, 616.
- (23) Miara, L. J.; Richards, W. D.; Wang, Y. E.; Ceder, G. First-Principles Studies on Cation Dopants and ElectrolytelCathode Interphases for Lithium Garnets. *Chem. Mater.* **2015**, *27*, 4040–4047.
- (24) Zhu, Y.; He, X.; Mo, Y. First principles study on electrochemical and chemical stability of solid electrolyte-electrode interfaces in all-solid-state Li-ion batteries. *J. Mater. Chem. A* **2016**, *4*, 3253–3266.
- (25) Lobe, S.; Bauer, A.; Sebold, D.; Wettengl, N.; Fattakhova-Rohlfing, D.; Uhlenbruck, S. Sintering of Li-garnets: Impact of Alincorporation and powder-bed composition on microstructure and ionic conductivity. *Open Ceram.* **2022**, *10*, 100268.
- (26) Roitzheim, C.; Sohn, Y. J.; Kuo, L.-Y.; Häuschen, G.; Mann, M.; Sebold, D.; Finsterbusch, M.; Kaghazchi, P.; Guillon, O.; Fattakhova-Rohlfing, D. All-Solid-State Li Batteries with NCM-Garnet-Based Composite Cathodes: The Impact of NCM Composition on Material Compatibility. ACS Appl. Energy Mater. 2022, 5, 6913–6926.
- (27) Bauer, A.; Ali, M. Y.; Orthner, H.; Uhlenbruck, S.; Wiggers, H.; Fattakhova-Rohlfing, D.; Guillon, O. Conductivity enhancement of Al- and Ta-substituted Li7La3Zr2O7 solid electrolytes by nanoparticles. *J. Eur. Ceram. Soc.* **2022**, *42*, 1033–1041.

- (28) Ikeda, Y.; Ito, H.; Matsumoto, G.; Hayashi, H. Thermal Stability of Lithium Aluminates by High Temperature Mass Spectrometry. J. Nucl. Sci. Technol. 1980, 17, 650–653.
- (29) Geiger, C. A.; Alekseev, E.; Lazic, B.; Fisch, M.; Armbruster, T.; Langner, R.; Fechtelkord, M.; Kim, N.; Pettke, T.; Weppner, W. Crystal Chemistry and Stability of "Li7La3Zr2O12" Garnet: A Fast Lithium-Ion Conductor. *Inorg. Chem.* **2011**, *50*, 1089–1097.
- (30) Kurinjimala, R.; Böhm, D.; Pessenhofer, W.; Eisenmenger-Sittner, C. Physical vapor deposited coatings on high Ni content NMC811 Li-ion battery cathode powder. *Surf. Coat. Technol.* **2023**, 462, 129472.
- (31) Forouzan, M. M.; Chao, C.-W.; Bustamante, D.; Mazzeo, B. A.; Wheeler, D. R. Experiment and simulation of the fabrication process of lithium-ion battery cathodes for determining microstructure and mechanical properties. *J. Power Sources* **2016**, *312*, 172–183.
- (32) Kondrakov, A. O.; Schmidt, A.; Xu, J.; Geßwein, H.; Mönig, R.; Hartmann, P.; Sommer, H.; Brezesinski, T.; Janek, J. Anisotropic Lattice Strain and Mechanical Degradation of High- and Low-Nickel NCM Cathode Materials for Li-Ion Batteries. *J. Phys. Chem. C* **2017**, 121. 3286–3294.
- (33) Placke, T.; Kloepsch, R.; Dühnen, S.; Winter, M. Lithium ion, lithium metal, and alternative rechargeable battery technologies: the odyssey for high energy density. *J. Solid State Electrochem.* **2017**, 21, 1939–1964.
- (34) Bitzer, M.; Van Gestel, T.; Uhlenbruck, S.; Hans-Peter-Buchkremer. Sol-gel synthesis of thin solid Li7La3Zr2O12 electrolyte films for Li-ion batteries. *Thin Solid Films* **2016**, *615*, 128–134.
- (35) Uhlenbruck, S.; Tietz, F. High-temperature thermal expansion and conductivity of cobaltites: potentials for adaptation of the thermal expansion to the demands for solid oxide fuel cells. *Mater. Sci. Eng. B* **2004**, *107*, 277–282.
- (36) Guo, H.; Li, Z. W.; Zhao, L.; Hu, Z.; Chang, C. F.; Kuo, C. Y.; Schmidt, W.; Piovano, A.; Pi, T. W.; Sobolev, O.; et al. Antiferromagnetic correlations in the metallic strongly correlated transition metal oxide LaNiO3. *Nat. Commun.* **2018**, *9*, 43.
- (37) Shannon, R. Revised effective ionic radii and systematic studies of interatomic distances in halides and chalcogenides. *Acta Crystallogr., Sect. A* **1976**, 32, 751–767.
- (38) Ida, J.-i.; Lin, Y. S. Mechanism of High-Temperature CO2 Sorption on Lithium Zirconate. *Environ. Sci. Technol.* **2003**, *37*, 1999–2004.
- (39) Gurvich, L. V.; Bergman, G. A.; Gorokhov, L. N.; Iorish, V. S.; Leonidov, V. Y.; Yungman, V. S. Thermodynamic Properties of Alkali Metal Hydroxides. Part 1. Lithium and Sodium Hydroxides. *J. Phys. Chem. Ref. Data* **1996**, 25, 1211–1276.
- (40) Stober, H. C. Lithium Carbonate. In *Analytical Profiles of Drug Substances*; Florey, K., Ed.; Academic Press, 1986; pp 367–391.
- (41) Urban, A.; Matts, I.; Abdellahi, A.; Ceder, G. Computational Design and Preparation of Cation-Disordered Oxides for High-Energy-Density Li-Ion Batteries. *Adv. Energy Mater.* **2016**, *6*, 1600488.
- (42) Cambaz, M. A.; Vinayan, B. P.; Euchner, H.; Johnsen, R. E.; Guda, A. A.; Mazilkin, A.; Rusalev, Y. V.; Trigub, A. L.; Gross, A.; Fichtner, M. Design of Nickel-Based Cation-Disordered Rock-Salt Oxides: The Effect of Transition Metal (M = V, Ti, Zr) Substitution in LiNi0.5M0.5O2 Binary Systems. ACS Appl. Mater. Interfaces 2018, 10, 21957–21964.
- (43) Pereira, M.; Peixoto, A. G.; Gomes, M. J. M. Effect of Nb doping on the microstructural and electrical properties of the PZT ceramics. *J. Eur. Ceram. Soc.* **2001**, *21*, 1353–1356.
- (44) Echigoya, J.; Hiratsuka, S.; Suto, H. Solid State Reaction of La(Co1-xNix)O3 with 10 mol%Y2O3-ZrO2. *Mater. Trans., JIM* 1989, 30, 789-799.
- (45) Goldschmidt, V. M. Die Gesetze der Krystallochemie. *Naturwissenschaften* **1926**, *14*, 477–485.
- (46) Geguzina, G. A.; Sakhnenko, V. P. Correlation between the lattice parameters of crystals with perovskite structure. *Crystallogr. Rep.* **2004**, 49, 15–19.
- (47) Levin, I.; Amos, T. G.; Bell, S. M.; Farber, L.; Vanderah, T. A.; Roth, R. S.; Toby, B. H. Phase equilibria, crystal structures, and

- dielectric anomaly in the BaZrO3-CaZrO3 system. J. Solid State Chem. 2003, 175, 170–181.
- (48) George, A. M.; Mishra, N. C.; Jayadevan, N. C. Synthesis of La2O3-stabilized cubic zirconia (La2/3ZrO3). *J. Mater. Sci. Lett.* **1992**, *11*, 404–406.
- (49) Lawson, S. M.; Greaves, G.; Blackburn, L. R.; Chapman, R.; Hyatt, N. C.; Corkhill, C. L. Synthesis and in situ ion irradiation of Asite deficient zirconate perovskite ceramics. *J. Mater. Chem. A* **2020**, 8, 19454–19466
- (50) Thangadurai, V.; Shukla, A. K.; Gopalakrishnan, J. LiSr1.650.35B1.3B'1.7O9 (B = Ti, Zr; B' = Nb, Ta): New Lithium Ion Conductors Based on the Perovskite Structure. *Chem. Mater.* **1999**, *11*, 835–839.
- (51) Huang, B.; Xu, B.; Li, Y.; Zhou, W.; You, Y.; Zhong, S.; Wang, C.-A.; Goodenough, J. B. Li-Ion Conduction and Stability of Perovskite Li3/8Sr7/16Hf1/4Ta3/4O3. ACS Appl. Mater. Interfaces 2016, 8, 14552–14557.
- (52) Yokokawa, H.; Sakai, N.; Kawada, T.; Dokiya, M. Thermodynamic stability of perovskites and related compounds in some alkaline earth-transition metal-oxygen systems. *J. Solid State Chem.* **1991**, *94*, 106–120.
- (53) Vieten, J.; Bulfin, B.; Huck, P.; Horton, M.; Guban, D.; Zhu, L.; Lu, Y.; Persson, K. A.; Roeb, M.; Sattler, C. Materials design of perovskite solid solutions for thermochemical applications. *Energy Environ. Sci.* **2019**, *12*, 1369–1384.
- (54) Sivaprakash, S.; Majumder, S. B. Understanding the role of Zr4+ cation in improving the cycleability of LiNi0.8Co0.15Zr0.05O2 cathodes for Li ion rechargeable batteries. *J. Alloys Compd.* **2009**, 479, 561–568.
- (55) Lipson, A. L.; Durham, J. L.; LeResche, M.; Abu-Baker, I.; Murphy, M. J.; Fister, T. T.; Wang, L.; Zhou, F.; Liu, L.; Kim, K.; et al. Improving the Thermal Stability of NMC 622 Li-Ion Battery Cathodes through Doping During Coprecipitation. ACS Appl. Mater. Interfaces 2020, 12, 18512–18518.
- (56) Liu, S.; Dang, Z.; Liu, D.; Zhang, C.; Huang, T.; Yu, A. Comparative studies of zirconium doping and coating on LiNi0.6Co0.2Mn0.2O2 cathode material at elevated temperatures. *J. Power Sources* **2018**, 396, 288–296.
- (57) Zheng, J.; Xiao, J.; Zhang, J.-G. The roles of oxygen non-stoichiometry on the electrochemical properties of oxide-based cathode materials. *Nano Today* **2016**, *11*, 678–694.
- (58) Niedrig, H. Electron backscattering from thin films. J. Appl. Phys. 1982, 53, R15-R49.
- (59) Howell, P. G. T.; Boyde, A. Monte Carlo simulation of electron backscattering from compounds with low mean atomic number. *Scanning* **1998**, *20*, 45–49.
- (60) Love, G.; Cox, M. G.; Scott, V. D. A versatile atomic number correction for electron-probe microanalysis. *J. Phys. D: Appl. Phys.* **1978**, *11*, 7–21.
- (61) Ksoll, P.; Mandal, R.; Meyer, C.; Schüler, L.; Roddatis, V.; Moshnyaga, V. Emergent double perovskite phase at LaMnO 3/LaNiO3 interfaces: Coupled charge transfer and structural reconstruction. *Phys. Rev. B* **2021**, *103*, 195120.
- (62) Koch, G.; Hävecker, M.; Teschner, D.; Carey, S. J.; Wang, Y.; Kube, P.; Hetaba, W.; Lunkenbein, T.; Auffermann, G.; Timpe, O.; et al. Surface Conditions That Constrain Alkane Oxidation on Perovskites. ACS Catal. 2020, 10, 7007–7020.
- (63) Scheld, W. S.; Lobe, S.; Dellen, C.; Ihrig, M.; Häuschen, G.; Hoff, L. C.; Finsterbusch, M.; Uhlenbruck, S.; Guillon, O.; Fattakhova-Rohlfing, D. Rapid thermal processing of garnet-based composite cathodes. *J. Power Sources* **2022**, *545*, 231872.
- (64) Ping, W.; Wang, C.; Wang, R.; Dong, Q.; Lin, Z.; Brozena, A. H.; Dai, J.; Luo, J.; Hu, L. Printable, high-performance solid-state electrolyte films. *Sci. Adv.* **2020**, *6*, No. eabc8641.
- (65) Sebastian Scheld, W.; Charlotte Hoff, L.; Vedder, C.; Stollenwerk, J.; Grüner, D.; Rosen, M.; Lobe, S.; Ihrig, M.; Seok, A. R.; Finsterbusch, M.; et al. Enabling metal substrates for garnet-based composite cathodes by laser sintering. *Appl. Energy* **2023**, 345, 121335.